Supplementary Information for

Mapping the Human Lateral Geniculate Nucleus and its Cytoarchitectonic Subdivisions Using Quantitative MRI

Christa Müller-Axt*, Cornelius Eichner, Henriette Rusch, Louise Kauffmann, Pierre-Louis Bazin, Alfred Anwander, Markus Morawski & Katharina von Kriegstein

*Corresponding Author:
Christa Müller-Axt
Email: muelleraxt@cbs.mpg.de

SI Methods

In-vivo MRI

LGN Segmentations on *In-vivo* Quantitative T_1 maps. Manual segmentation of bilateral LGNs were performed by two independent raters on the N=27 high-resolution *in-vivo* qT_1 maps. In order to standardize the segmentation procedure between raters and across participants, we first computed a histogram of T_1 relaxation values (number of bins=1000, bin width=4ms) from each participants' qT_1 map. Each histogram was then convolved with a Gaussian filter with sigma=20ms to reduce local signal-to-noise fluctuations. The resulting histograms yielded two clear global peaks, corresponding to the T_1 relaxation peaks in gray and white matter in each participant. The T_1 relaxation peaks were extracted and subsequently used as windowing parameters for the manual LGN segmentations. Specifically, for each segmentation, the minimum intensity of the qT_1 maps was set to the participant-specific white matter T_1 relaxation peak, while the maximum intensity was set to the participant-specific gray matter T_1 relaxation peak. This was done to optimize the visibility of the LGN and to ensure that all LGN segmentations were based on a similar gray-white matter contrast. The order in which the left or right LGN was segmented was randomized per participant.

Group Template Generation and LGN Population Atlas. To normalize the bilateral LGN masks to a common reference space, we first created a study-specific group template from the N=27 individual high-resolution qT_1 maps. The qT_1 group template was generated using the *buildtemplateparallel.sh* script implemented in the Advanced Normalization Tools (ANTs, version 2.1.0) software package. The study-specific group template was built in two steps: First, all qT_1 images were affine registered using default parameters and averaged to create a globally aligned initial template. This initial template subsequently served as registration target in the first of a total of four iterations of full deformable registration used to create the qT_1 group template. Full deformable registration was run with symmetric normalization diffeomorphic image registration (SyN) as transformation model, cross-correlation as similarity metric, and default Gauss regularization [3, 0.5] of the deformation field. Mapping parameters for the SyN transformation model were chosen according to the suggestions in Avants et al. (2011). Specifically, the gradient step length was set to 0.5, the number of time discretization points was set to 2, and the integration time step was set to 0.05. Given the high resolution of the qMRI data, the deformable registration was run at five different levels of image resolution (from coarse to fine), with downsampling factors of 2^n with n = [4, 3, … 0]. At each image resolution level, the maximum number of iterations was set to n_{max_iter} = [400, 200, 100, 50, 20]. A total of four iterations of full deformable registration were employed, where each iteration built on the intermediate group template (set as new registration target) and deformed individual data of

the previous iteration. The obtained linear and nonlinear registration parameters of the last iteration were then applied to the N=27 qT_1 maps using linear interpolation, and all registered images were averaged to create the qT_1 group template (Fig. S1a-c and Fig. 1a). Finally, the same registration parameters were applied to the conjoined LGN masks using linear interpolation, followed by averaging of the registered masks within each hemisphere to create a bilateral LGN population atlas (Fig. 1b and Fig. 2a & b).

Cross-Validation of LGN Population Atlas. To assess the prediction accuracy of the bilateral LGN population atlas, we performed a four-fold cross-validation procedure. For cross-validation, four new qT_1 group templates were created based on subsets of the data. The four qT_1 templates were built in ANTs using the same procedures as described for generating the full N=27 study-specific qT_1 group template. Each subset consisted of approximately 75% of the whole qT_1 dataset: $N_{fold1\text{-}3}$=20 participants and N_{fold4}=21 participants. For each subset, the corresponding LGN population atlases were additionally computed. The LGN population atlases were subsequently used to predict the location of the LGN in the remaining participants. Subsets were created pseudo-randomly, such that every participant's LGN was predicted exactly once. Next, the LGN population atlases were warped to the single-subject qT_1 maps using SyN in ANTs. For each hemisphere and participant, thresholds were then applied to the registered LGN population atlases (in increments of 5% overlap) until they matched the mean LGN volume across all N=27 participants in the respective hemisphere as closely as possible (for comparison, mean LGN volume left = 113.5mm^3, mean LGN volume right = 120.9mm^3). Dice coefficients were calculated between the resulting LGN population atlases and the manually segmented LGN masks in each participant. Finally, Dice coefficients were averaged (weighted by fold size) across participants for each hemisphere. The four-fold cross-validation revealed a good prediction accuracy of the bilateral LGN population atlas on a single-subject level with mean Dice coefficients of 0.80±0.07 and 0.83±0.04 in the left and right hemisphere, respectively.

Monte Carlo Simulations on Separability Index. As both subdivisions of the LGN constitute part of the same underlying tissue class (i.e., subcortical gray matter), we cannot expect full separability between them. To numerically assess under which conditions the LGN subdivisions are separable given the employed model, D, we performed Monte Carlo simulations. For this, synthetic T_1 distributions with an 80/20 volumetric contribution (Andrews et al., 1997) of parvocellular/magnocellular subcomponents were synthesized using the employed model. The synthetic distributions were generated across 30 equidistant separability indices ranging from ϑ = 0 (overlapping distributions with no separability) to ϑ = 3 (high separability). The distributions were then contaminated with 20 equidistant levels of Gaussian

noise, ranging from 10% to 100% intensity of the simulated P component, i.e., SNR_{max} = 10 to SNR_{min} = 1 (Figure S2a). The model D was then fitted to 1000 representations of the synthesized noisy distributions without any boundary conditions, using the SciPy function 'curve_fit'. For each combination of ϑ and noise level, the number of occurrences of misclassified M and P components in the model fit was assessed. The Monte Carlo simulations revealed a large number of misclassifications for $\vartheta < 1$ (i.e., 44.6±8.5%). For $\vartheta \geq 1$, the number of model-fit derived misclassifications was substantially reduced (13.7±9.0%; Figure S2b). In cases of $\vartheta \geq 1$, the model was able to identify subcomponents, even without the help of boundary conditions. As a consequence of the Monte Carlo simulation results, only model fits with $\vartheta \geq 1$ were judged as separable.

Post-Mortem MRI and Histology

HuC/D and MBP Immunohistochemistry. For histological examination, the LGN tissue block was cryoprotected in 30% sucrose and cut into 30µm consecutive sections using a Jung Histoslide 2000 freezing microtome (Leica, Wetzlar, Germany) equipped with a Hyrax 30 freezing unit (Carl Zeiss, Jena, Germany). The LGN comprised 5.4mm (180 sections from posterior to anterior pole) in total. Every seventh 30µm section was used for a series of immunohistochemical stains to cover the LGN in slices compatible with the *post-mortem* MR acquisition resolution (immunohistochemistry: 7x30µm = 210µm; MR acquisition resolution = 220µm). After washing the free-floating slices in phosphate-buffered saline with Tween (PBS-Tween), slices were pre-treated for antigen retrieval following previously published procedures (Morawski et al., 2012). Afterwards, another washing step was employed, and samples were incubated in blocking solution (2% bovine serum albumin (BSA), 0.3% milk powder and 0.5% donkey normal serum (DNS) in PBS) for 1h at room temperature to avoid unspecific binding of antibodies. Next, slices were incubated with primary antibodies, HuC/D (mouse; 1:500; A21271; ThermoFisher Scientific, Waltham, MA, USA) or MBP (rat; 1:400; NB600-717; Novus Biologicals, Littleton, CO, USA) for 48h at 4°C in blocking solution. Subsequently, sections were washed in PBS-Tween and incubated for 1h in biotinylated secondary antibody solution (donkey-anti-mouse or donkey-anti-rat; 1:1000; Dianova, Hamburg, Germany) containing PBS-Tween and blocking solution (1:2). Again, sections were washed in PBS-Tween and incubated in streptavidin (1:2000; Extravidin®; Sigma Aldrich, St. Louis, MO, USA). After washing in PBS-Tween and Tris-Hydrochloride (Tris-HCl; pH 8.0), samples were batch-wise developed in 3,3'-Diaminobenzidine (DAB; Sigma Aldrich) and nickel-ammonium sulphate (Sigma Aldrich) for 3min under visual control. Last washing steps were performed with Tris-HCl (pH 8.0) and PBS before samples were mounted onto microscopic slides, air-dried and coverslipped with Entellan® (Merck, Darmstadt, Germany).

Perls' Prussian Blue Histochemistry. Cryo-cut 30µm samples were mounted onto microscopic slides and air-dried overnight. Sections were then washed in distilled and double-distilled water. Perls' Prussian blue solution consisted of 1:1 freshly mixed 5% potassium hexacyanoferrate-II and 5% hydrochloric acid. Samples were immersed and incubated at 37°C for 2h (Perls, 1867; Stüber et al., 2014). Samples were then washed in phosphate-buffered saline (PBS) and Tris-Hydrochloride (Tris-HCl; pH 8.0) and for intensification of stain developed in 3,3'-diaminobenzidine (DAB; Sigma Aldrich, St. Louis, MO, USA) and nickel-ammonium sulphate (Sigma Aldrich) for up to 20min under visual evaluation. Samples were subsequently washed in Tris-HCl (pH 8.0), PBS and distilled water. Finally, after undergoing ascending dehydration and processing with toluol, samples were coverslipped with Entellan® (Merck, Darmstadt, Germany).

LGN Layer Tracing and Labeling. Individual LGN layers were manually traced using the polygon drawing tool of Zeiss ZEN 2.0 lite software (Carl Zeiss, Jena, Germany). Immunohistochemical staining of neuronal cell body marker anti-HuC/D showed best differentiation between layers; and was thus used for initial manual layer tracing and as a template for tracing on the other markers (i.e., anti-MBP and Perls' Prussian blue). Interlaminar koniocellular layers provided visual guidance in separating individual M and P layers. In addition, a previous comprehensive study on human LGN laminar arrangements (Hickey and Guillery, 1979) served as anatomical guideline for layer tracing and labeling. In posterior parts of the nucleus, the laminar arrangement of the LGN may deviate from the typically described six-layered structure towards a four-layer LGN segment (Hickey and Guillery, 1979). This was also the case in the current sample. This four-layer LGN segment comprised two ventral M layers and two dorsal P layers, in which ipsilateral layers P3/5 and contralateral layers P4/6 are fused in pairs (Hickey and Guillery, 1979). We therefore calculated histological measures for the two fused P layers (i.e., layers P3/5 and P4/6) and each of the two ventral M layers.

Cell Density and Optical Density Analyses. A stereological analysis of cell density was performed on the immunohistochemical staining of neuronal cell body marker anti-HuC/D. Cell density in each traced LGN layer was approximated by a cell body count within six uniformly distributed equally sized squares of 60191 μm^2 in each of the two fused LGN P layers and in each of the two LGN M layers. This was done using the 'Image Analysis' module, as implemented in the Zeiss ZEN software (version 2.6; Carl Zeiss, Jena, Germany). This procedure resulted in six cell count measures per (fused) LGN layer, which were subsequently normalized by area to approximate the cell density in each respective LGN layer.
For the optical density analyses of the anti-MBP and Perls' Prussian blue markers, values of mean intensities were extracted per traced (fused) LGN layer through the Zeiss ZEN 2.0 lite

software. Normalized optical density measures were then computed by subtraction of the mean intensity from the individual background reference, as measured at an unstained tissue part within a standardized square of 20 μm^2. This procedure resulted in exactly one normalized optical density measure for each of the two fused LGN P layers and each of the two LGN M layers on the sections stained with anti-MBP or Perls' Prussian blue. To provide a measure of the variability within layers, the mean and standard deviation of the optical density of anti-MBP and PB per layer were additionally approximated in N=6 uniformly distributed equally sized squares of 60191 μm^2.

SI Figures

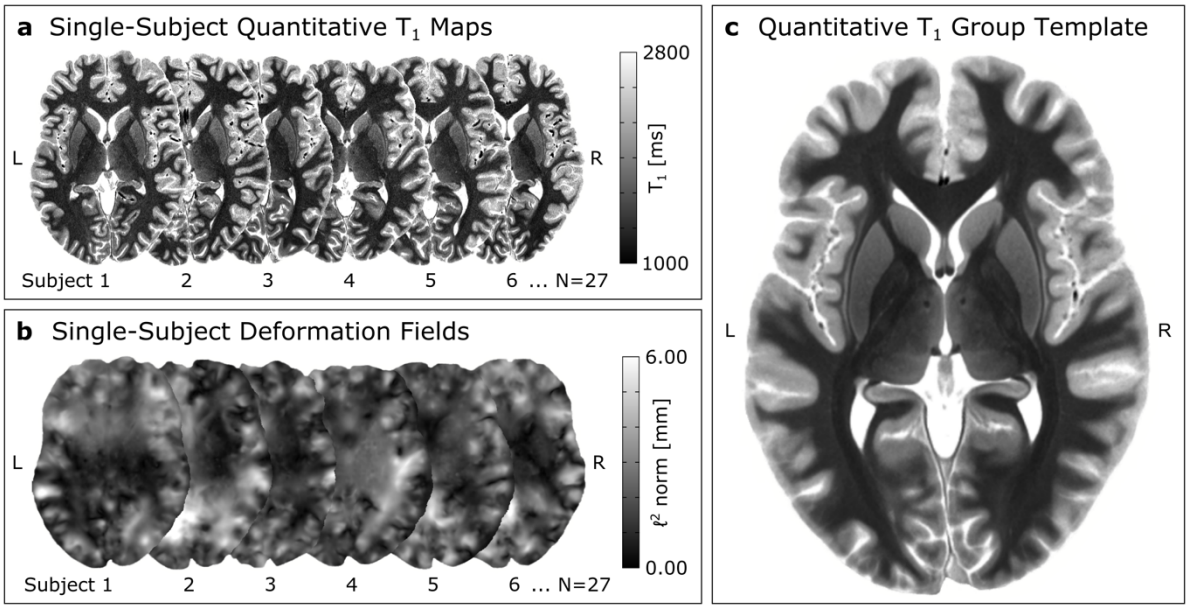

Fig. S1. Workflow for creating the study-specific quantitative qT_1 group template. **(a)** A total of N=27 single-subject whole-brain qT_1 maps served as input for symmetric normalization image registration (SyN) in ANTs. Image intensities of the single-subject qT_1 maps indicate the longitudinal relaxation time T_1 (in ms) per voxel. **(b)** Four iterations of SyN registration yielded a deformation field for each of the input images, describing the respective voxel displacement for each spatial dimension. For visualization purposes, we here show the Euclidean norm (in mm) of the estimated 3D deformation fields per voxel. **(c)** Following quality control, the deformation fields were applied to the single-subject qT_1 maps, and all registered images were averaged to create a study-specific qT_1 group template.

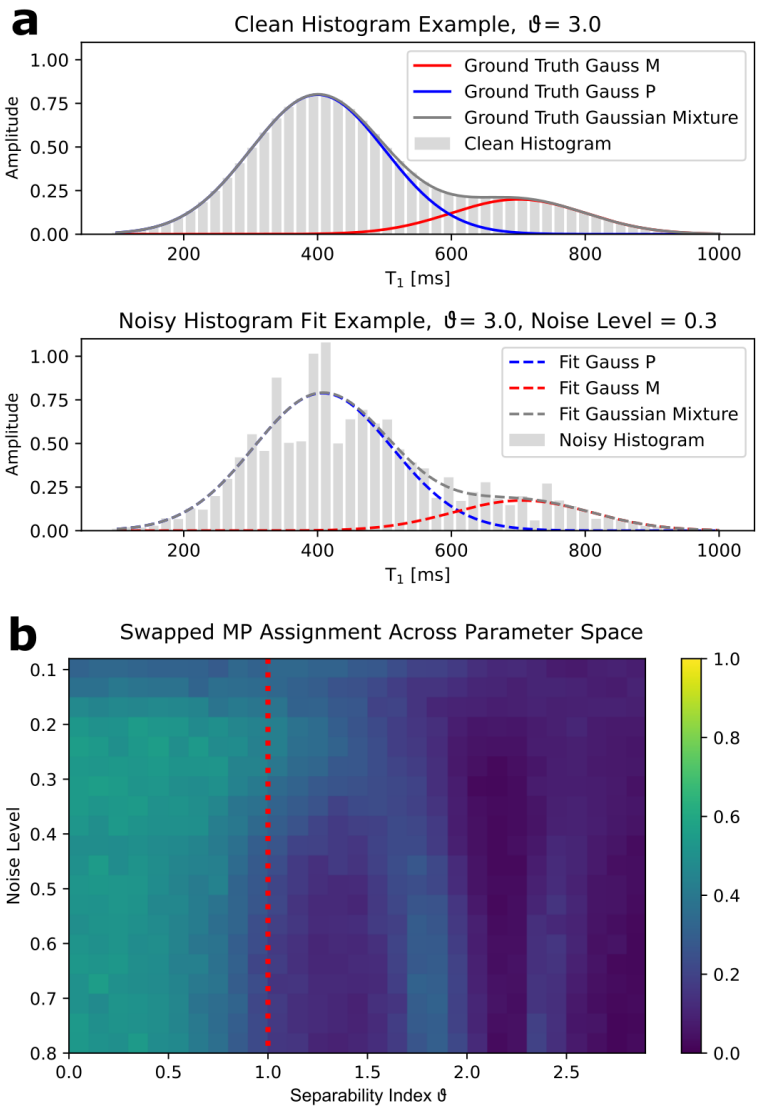

Fig. S2. Monte Carlo simulations on the separability index. **(a)** Example of synthesized noisy T_1 distribution. In line with classic anatomical studies, the amplitudes for the parvocellular and magnocellular components were chosen to be 0.8 and 0.2, respectively. Synthetic T_1 distributions were generated for various separability indices. For a given distribution D, the separability index alone sufficiently describes the shape for a given set of amplitudes, making the absolute underlying T_1 values irrelevant. For each ϑ, 1000 noisy distributions were generated using a normally distributed noise vector, following N~(1,Noise Level). The noise level was derived from the SNR of the target distribution based on the intensity of the parvocellular peak. **(b)** Proportion of M/P misclassifications for a given theta and noise level. The Monte Carlo simulations revealed that a separability index of $\vartheta \geq 1$ can separate LGN subdivisions with sufficient accuracy (red dotted line indicates $\vartheta = 1$) across a wide range of noise levels.

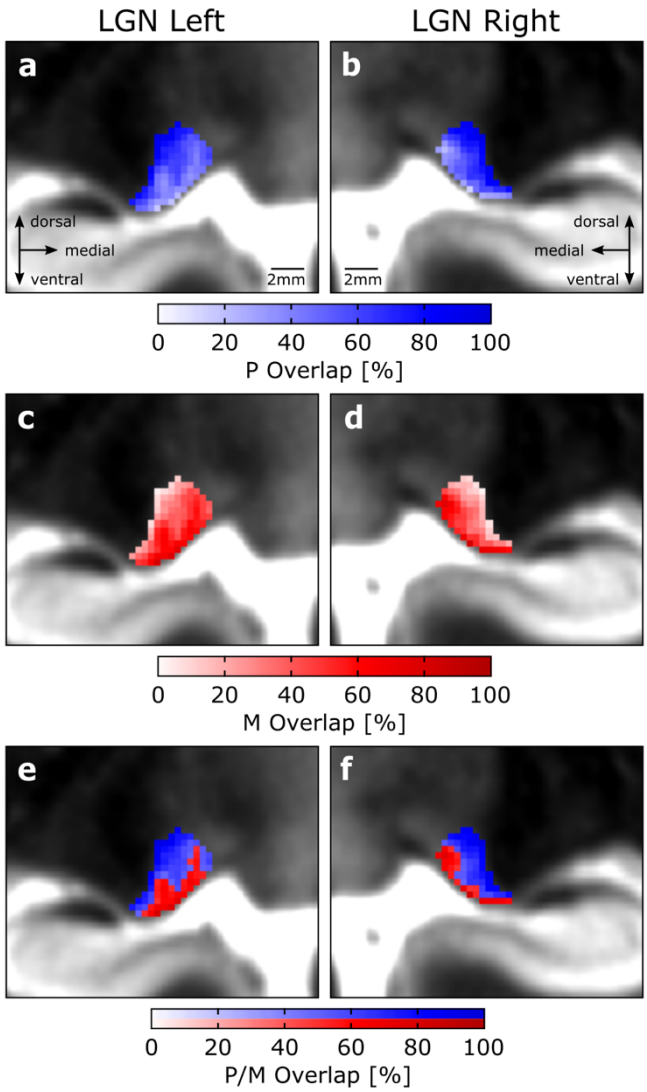

Fig. S3. *In-vivo* LGN subdivisions based on model fits with $\vartheta \geq 1$. Population maps are overlaid on a slice of the study-specific qT_1 group template in coronal view. Displayed voxel dimensions correspond to 0.4mm isotropic image resolution. **(a-b)** Population atlas of the left (a) and right (b) LGN P subdivision based on N=14 and N=18 participants, respectively. Color coding indicates the overlap in P-classified voxels across participants. **(c-d)** Population atlas of the left (c) and right (d) LGN M subdivision based on N=14 and N=18 participants, respectively. Color coding indicates the overlap in M-classified voxels across participants. **(e-f)** Left (e) and right (f) LGN P and M subdivision population maps, set to a threshold of at least 50% overlap across participants. The blue-shaded part of the color bar indicates the overlap for the dorsal P subdivision, while the red-shaded part of the color bar indicates the overlap for the ventral M subdivision. **(a-f)** Population maps are shown for voxels of the probabilistic LGN atlas (Fig. 1b & Fig. 2a, 2b) with at least 50% overlap across subjects.

SI References

Andrews, T.J., Halpern, S.D., Purves, D., 1997. Correlated size variations in human visual cortex, lateral geniculate nucleus, and optic tract. J. Neurosci. 17, 2859–2868.

Avants, B.B., Tustison, N.J., Song, G., Cook, P.A., Klein, A., Gee, J.C., 2011. A reproducible evaluation of ANTs similarity metric performance in brain image registration. NeuroImage 54, 2033–2044.

Hickey, T.L., Guillery, R.W., 1979. Variability of laminar patterns in the human lateral geniculate nucleus. J. Comp. Neurol. 183, 221–246.

Morawski, M., Brückner, G., Jäger, C., Seeger, G., Matthews, R.T., Arendt, T., 2012. Involvement of perineuronal and perisynaptic extracellular matrix in Alzheimer's disease neuropathology. Brain Pathol. 22, 547–561.

Perls, M., 1867. Nachweis von Eisenoxyd in gewissen Pigmenten. Arch. für Pathol. Anat. und Physiol. und für Klin. Med. 39, 42–48.

Stüber, C., Morawski, M., Schäfer, A., Labadie, C., Wähnert, M., Leuze, C., Streicher, M., Barapatre, N., Reimann, K., Geyer, S., Spemann, D., Turner, R., 2014. Myelin and iron concentration in the human brain: a quantitative study of MRI contrast. NeuroImage 93, 95–106.